Characterization of spatial porosity and mineral distribution of crystalline rock using X-ray micro computed tomography, C-14-PMMA autoradiography and scanning electron microscopy

Mikko Voutilainen[a,*], Arttu Miettinen[b,c], Paul Sardini[d], Joni Parkkonen[b], Juuso Sammaljärvi[a], Björn Gylling[e], Jan-Olof Selroos[e], Maarit Yli-Kaila[f], Lasse Koskinen[f], Marja Siitari-Kauppi[a]

[a] Department of Chemistry, University of Helsinki, Helsinki, 00014, Finland
[b] Department of Physics, University of Jyväskylä, Jyväskylä, 40014, Finland
[c] Swiss Light Source, Paul Scherrer Institute, Villigen, 5234, Switzerland
[d] Institute of Chemistry, University of Poitiers, Poitiers, 86022, France
[e] Swedish Nuclear Fuel and Waste Management Company, Solna, 169 03, Sweden
[f] Posiva Oy, Eurajoki, 27160, Finland

ARTICLE INFO

ABSTRACT

The spatial porosity and mineral distribution of geological materials strongly affects transport processes in them. X-ray micro computed tomography (X-μCT) has proven to be a powerful tool for characterizing the spatial mineral distribution of geological samples in 3-D. However, limitations in resolution prevent an accurate characterization of pore space especially for tight crystalline rock samples and 2-D methods such as C-14-polymethylmethacrylate (C-14-PMMA) autoradiography and scanning electron microscopy (SEM) are needed. The spatial porosity and mineral distributions of tight crystalline rock samples from Äspö, Sweden, and Olkiluoto, Finland, were studied here. The X-μCT were used to characterize the spatial distribution of the main minerals in 3-D. Total porosities, fracture porosities, fracture densities and porosity distributions of the samples were determined using the C-14-PMMA autoradiography and characterization of mineral-specific porosities were assisted using chemical staining of rock surfaces. SEM and energy dispersive X-ray spectroscopy (EDS) were used to determine pore apertures and identify the minerals. It was shown that combination of the different imaging techniques creates a powerful tool for the structural characterization of crystalline rock samples. The combination of the results from different methods allowed the construction of spatial porosity, mineral and mineral grain distributions of the samples in 3-D. These spatial distributions enable reactive transport modeling using a more realistic representation of the heterogeneous structure of samples. Furthermore, the realism of the spatial distributions were increased by determinig the densities and porosities of fractures and by the virtual construction heterogeneous mineral distributions of minerals that cannot be separated by X-μCT.

1. Introduction

In recent years, the rapid development of X-ray computed tomography techniques has enabled a micrometer-level resolution in the routine 3-D imaging of geological materials (Ketcham and Carlson, 2001; Schladitz, 2011; Cnudde and Boone, 2013; Fusseis et al., 2014), and even nanometer scale resolution is now possible with limited sample size (Bugani et al., 2007; Kuva et al., 2015a). The X-ray computed tomography has proven to be a powerful technique in geosciences for resolving spatial mineral distribution in 3-D (Denison and Carlson, 1997; Kahl et al., 2017) and, in some cases, pores and fractures (Ketcham et al., 2010; Schmitt et al., 2016; Lai et al., 2017; Latief et al., 2017). However, in tight crystalline rocks, part of pores remain undetected using the X-ray micro computed tomography (X-μCT) techniques as the size of pore apertures lie below the detection limit for centimeter scale samples that are often studied (Mazurier et al., 2016).

In order to resolve the pore structure of crystalline rock samples, the X-μCT must be combined with more accurate 2-D analysis methods. The C-14-PMMA autoradiography has been found to be applicable when studying the pore structure and spatial porosity distribution of centimeter scale samples (Hellmuth et al. 1993, 1994; Siitari-Kauppi, 2002). During the past decade, the method has been used to investigate

---

LTDE-SD-GDR1   LTDE-SD-GDR2   REPRO-VGN   REPRO-PGR
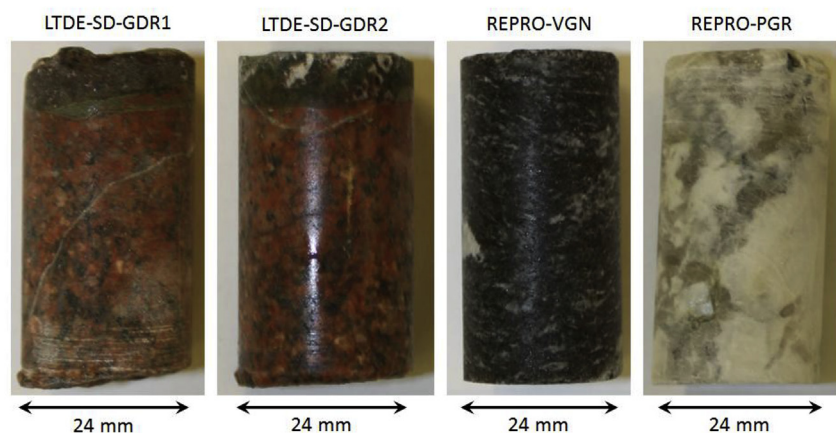
24 mm   24 mm   24 mm   24 mm

Fig. 1. The Äspö granodiorite samples LTDE-SD-GDR1 and LTDE-SD-GDR2 were collected from the experimental site of LTDE-SD, and Olkiluoto veined gneiss (REPRO-VGN) and pegmatitic granite (REPRO-PGR) from the experimental site of the REPRO-project. The diameter of the samples was 24 mm and the length from 43 mm to 48 mm.

the porosity and pore structure e.g. of crystalline rock (Kelokaski et al., 2006; Sardini et al., 2006), clay rock (Robinet et al., 2015), bentonite (Prêt et al., 2010) and cement (Lalan et al., 2016). Furthermore, the recent developments of autoradiographic techniques and polymerization methods have widened the applicability of the method (Sammaljärvi et al., 2012; Sardini et al. 2015, 2016; Kuva et al., 2015b; Voutilainen et al., 2018). The C-14-PMMA autoradiography, however, offers only averaged information on local porosity from micrometer and nanometer scales and thus other methods have to be applied to have quantitative information about pore apertures at these scales. However, recent methodological developments propose new approaches to determining fracture apertures and densities using C-14-PMMA autoradiography (Sardini et al., 2014; Kuva et al., 2015a,b,c; Mazurier et al., 2016). Furthermore, scanning electron microscopy (SEM) has been found to be a powerful tool (Pittman and Thomas, 1979; Anselmetti et al., 1998) to evaluate pore apertures and energy dispersive X-ray spectroscopy (EDS) connected to SEM can be applied for the identification of minerals and their alteration products (e.g. clays).

Combination of the X-μCT, C-14-PMMA autoradiography and SEM-EDS has been found to be a powerful tool for characterizing the spatial porosity and mineral distribution of rock samples adjacent to water conducting fractures (Kuva et al., 2012), highly altered crystalline rock (Voutilainen et al., 2012), and clay rock (Robinet et al., 2012). The combination of these methods has found to be advantageous as a wider range of the length scales of the structural features is being covered than when using only one method. Furthermore, the resulting 3-D mineral and porosity distributions have been used directly in reactive transport modeling that takes into account the local geochemical conditions (Voutilainen et al. 2013, 2017; Iraola et al., 2017).

The spatial porosity and mineral distribution of geological materials strongly affect the transport processes (e.g. diffusion and sorption) in them. One particularly timely application, where the migration processes in crystalline rock plays an important role, is the geological disposal of spent nuclear fuel. In the safety assessment of deep geological repositories in geological formations, it is important to consider scenarios where long-lived radionuclides are released from the fuel canisters to the geosphere. In order to obtain transport parameters representative of in situ conditions in deep geological repositories, Swedish and Finnish spent nuclear fuel management companies (i.e. SKB and Posiva) have performed series of in situ transport experiments in Äspö, Sweden, and Olkiluoto, Finland (Nilsson et al., 2010; Voutilainen et al., 2014). The experiments have shown anomalous results and it has not been possible to fully explain the results of these experiments using simple models that assume a homogeneous rock (Widestrand et al., 2010a; Poteri et al., 2018). Currently, these results are being assessed by an international team of experimentalists and modelers in the SKB Task Force on Groundwater Flow and Transport of Solutes (www.skb.se/taskforce). An explanation for the anomalous

results could be the heterogeneous pore and mineral distribution of crystalline rock that affects the reactive transport of radionuclides. Recently, it has been shown that the fractures, reactive grains and intra-granular porosity have a conjoint and distinct role of for understanding the transport of radionuclides in crystalline rock matrices (Sardini et al., 2007; Trinchero et al., 2017; Park and Ji, 2018).

The aim of this study is to produce data on the heterogeneous pore and mineral distribution of crystalline rock so that modelers can apply realistic structures in their models that take into account spatially varying geochemical properties. To this end, the X-μCT, C-14-PMMA autoradiography and SEM-EDS were combined in this study to properly characterize the heterogeneous mineral and pore distribution of crystalline rock samples from Äspö and Olkiluoto. Combining the results of these different methods, spatial porosity and mineral distributions were constructed for the crystalline rock samples in 3-D. Such spatial distributions will enable us to model the reactive transport of radionuclides in crystalline rock samples in a more realistic manner and give a possibility to explain the anomalous results of in situ experiments. The aim has also been to demonstrate that the characterization methods can be used to construct the spatial porosity and mineral distributions of crystalline rock samples more accurately than in previous studies by integrating in the 3-D model the fracture porosity obtained by C-14-PMMA autoradiography. Such developments increase the realism of these 3-D spatial distributions and enable novel approaches for reactive transport modeling.

2. Materials and methods

2.1. Rock samples

The granodiorite (GDR) samples studied here were taken from the \"Asp\"o Hard Rock Laboratory (HRL) in Sweden. The drill core samples LTDE-SD-GRD1 and LTDE-SD-GRD2 with diameter of 24 mm and length of 43 mm were drilled from an exposed fracture surface, and were part of the Long Term Diffusion and Sorption Experiment (LTDE-SD) (Nilsson et al., 2010; Widestrand et al., 2010a). The rock samples include a fracture coating, an alteration rim with thickness of about 5 mm and the underlying less altered rock matrix (see Fig. 1). The fracture coating consists of calcite and quartz together with minor amounts of chalcopyrite and small crystals of barite and fluorite, and the alteration rim consists mainly of epidote and chlorite (Widestrand et al., 2010b). The less altered rock matrix is fine-grained and slightly foliated and it consists mainly of quartz, plagioclase, K-feldspar and mica minerals (see Table 1) (Widestrand et al., 2010b). The samples studied by Widestrand et al. (2010b) have shown that plagioclase is partly saussuritised and sericitised, and mica minerals are chlorite that is altered from biotite. Total connected porosity of (0.26 ± 0.08) % has been determined for the rock matrix using water saturation method and

Table 1
Abundances of main minerals in Äspö granodiorite (GRD), Olkiluoto Veined gneiss (VGN), and Olkiluoto pegmatitic granite (PGR) (Widestrand et al., 2010b; Ikonen et al., 2015).

Mineral	Äspö GRD	Olkiluoto VGN	Olkiluoto PGR
Quartz	35.2	28.1	47.6
Plagioclase	26.2	14.2	31.5
K-feldspar	31.8	15.0	16.5
Mica minerals[a]	5.0	29.3	3.4

[a] Mica minerals include here biotite, chlorite and muscovite.

it has been shown that the majority of the porosity is located at the grain boundaries around quartz and feldspar grains, and in biotite grains (Widestrand et al., 2010b).

The veined gneiss (REPRO-VGN) and pegmatitic granite (REPRO-PGR) samples studied here were taken from the Underground characterization and research facility (ONKALO) in Olkiluoto, Finland. The drill core samples REPRO-VGN and REPRO-PGR (see Fig. 1) with diameter of 24 mm and length of 47 mm (REPRO-PGR) and 48 mm (REPRO-VGN) were drilled from the experimental site of "rock matrix REtention PROperties" -project (REPRO) during the drilling campaign (Toropainen, 2012). The total connected porosities of (0.7 ± 0.2) % and (0.6 ± 0.2) % were measured for REPRO-VGN and REPRO-PGR samples in average, respectively, using helium gas pycnometry (Kuva et al., 2015c). The petrography of the samples from the REPRO site have been extensively studied by (Ikonen et al., 2015) and by (Sammaljärvi et al., 2017). Their results show that main minerals of the samples are quartz, plagioclase, K-feldspar and various mica minerals (see Table 1). In the REPRO-VGN sample the mica minerals were mostly biotite and lesser amounts of muscovite. The sample contained also partly pinitized cordierite, sillimanite, kaolinite and illite as accessory minerals. In the REPRO-PGR sample the mica minerals were mostly muscovite with garnet, illite and kaolinite as accessory minerals. The REPRO-VGN sample was found to be fine grained and foliated whereas the REPRO-PGR sample was medium to coarse grained and non-foliated (see Fig. 1).

The samples (LTDE-SD-GRD1, REPRO-VGN and REPRO-PGR) were first scanned with the X-μCT. After impregnation with C-14-MMA and polymerization to C-14-PMMA, all samples were sawed into two pieces so that the first half was analyzed using the C-14-PMMA autoradiography and chemical staining of minerals, and the second half was analyzed using SEM-EDS.

2.2. X-ray micro computed tomography

The 3-D mineral distributions of the samples were resolved using the X-ray micro computed tomography (X-μCT) method that is based on detecting the difference in local X-ray attenuation between different parts of the sample (Ketcham and Carlson, 2001). The 3-D mineral distributions of the three samples (LTDE-SD-GRD1, REPRO-VGN and REPRO-PGR) were resolved using a SkyScan 1172 X-μCT scanner. The scanner is based on a microfocus X-ray tube with an approximately 5 μm X-ray source size and a conical X-ray beam. The samples were scanned using a voxel size of 13.58 μm, an acceleration voltage of 100 kV and an electron beam current of 80 μA. Aluminum and copper filters (1 mm thick) were used to treat the X-ray energy spectra. After the treatment the maximum intensity of the spectra was at 59 keV (Kα energy of tungsten) and the maximum energy was 100 keV. A total of 2040 projection images were recorded during the scan with a rotation step of 0.10°. The reconstruction of the 3-D image was done using the Feldkamp algorithm (Feldkamp et al., 1984) implemented in a commercial software (SkyScan NRecon). Suitable alignment, beam hardening, and ring artefact corrections were used.

In order to analyze the mineral distributions of the samples, the tomographic images were denoised, the various material phases were segmented from each other and the distributions of each mineral phase were analyzed separately. First a non-linear variance-based noise-reduction filter (Gonzalez and Woods, 2002) was used to denoise the 3-D X-μCT images. Before further processing, the LTDE-SD-GRD1 sample was segmented into two sub-samples: the first one contained the alteration rim and the second one contained the less altered rock matrix. The interface between the two parts was found using the Carpet algorithm (Turpeinen et al., 2015). The REPRO-VGN and the REPRO-PGR samples were processed as-is. The applied image processing tools were in-house built plugins for ImageJ. After denoising was done for the full X-μCT images, the histograms of the images were determined. The different mineral phases could be identified in the histograms as separate peaks. Threshold values for segmentation of each phase were decided such that the thresholds were in between the peaks. Finally the images were thresholded, yielding an image where the value of a pixel indicates the phase it belongs to. To make a virtual grain segmentation of each phase, an in-house built plugin for ImageJ applying the watershed algorithm was used (Gonzalez and Woods, 2002). The volume of each grain was determined and the volume distribution of grains was drawn for each phase. The grain volume distribution was converted to a grain size distribution using the diameter of equivalent spheres (i.e. grain size was taken to be the diameter of a sphere whose volume equals the volume of the grain). Grain boundaries were also extracted from the grain images using the variance operator, and subsequent topological skeletonization using an in-house built plugin for ImageJ. These boundaries represent the network of fractures and grain boundaries that exists in the crystalline rock. Fracture density (fracture surface per unit volume) were determined from these 3-D images.

2.3. Scanning electron microscopy

In order to have structural information on micrometer scale, to identify the minerals and their alteration products (e.g. clays) in the samples, the samples were analyzed using a field emission scanning electron microscope (FE-SEM) Hitachi S-4800 model with Oxford instruments X-sight X-ray diffractometer (EDS). The FE-SEM-EDS was used in high vacuum mode with COMPO back scattered signal, 20 kV accelerating voltage and 1 nA probe current. The FE-SEM-EDS system was operated by Oxford Instruments INCA and AZtec softwares and the semiquantitative analytical data obtained for elemental composition was normalized to 100%.

2.4. C-14-PMMA autoradiography

The total connected porosity and spatial porosity distribution of the samples were resolved using the C-14-PMMA autoradiography (Hellmuth et al. 1993, 1994; Siitari-Kauppi, 2002). The mean range of beta particles emitted by C-14 is about 20 μm in crystalline rock and thus features below this range are not seen as discrete features in the spatial distribution of porosity. However, as C-14-MMA has low molecular weight and low viscosity, it intrudes into nanometer scale pores and the value for local porosity represents the average porosity within a radius of 20 μm. All open fractures and grain boundaries, regardless their aperture, are detected using C-14-PMMA autoradiography. In the autoradiograph, a planar features (such as fractures and grain boundaries) are continuous series of point sources and they can be seen as lines with higher activity and porosity than the surrounding rock (Sardini et al., 2014).

The samples were first dried in a vacuum oven (105 °C) for 14 days and impregnated in vacuum for 30 days using a C-14-MMA solution with initial activity of 895 kBq/ml. The impregnation was followed by polymerization of C-14-MMA to C-14-PMMA in heat bath using azobisisobutyronitrile as a thermal initiator (Sammaljärvi et al., 2012). After polymerization, the samples sawed, the studied rock surfaces were polished and spatial distribution of C-14-PMMA on the surfaces were
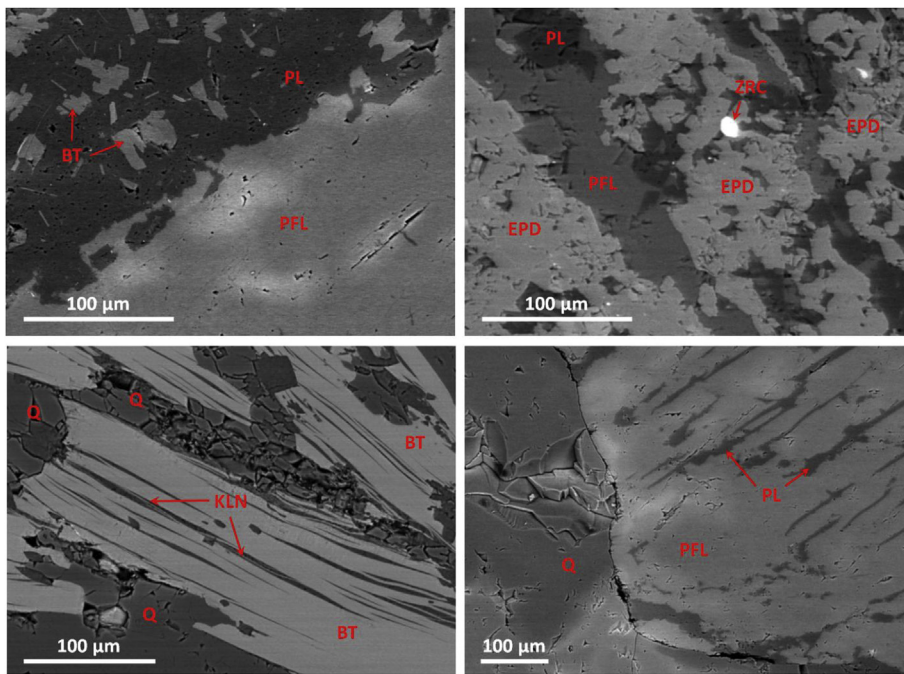
Fig. 2. The BSE images from FE-SEM show the typical mineral grains and pores in alteration rim (upper right panel) and rock matrix (upper left panel) of LTDE-SD-GRD1, REPRO-VGN (lower left panel), and REPRO-PGR (lower right panel). The minerals in the samples were identified using EDS coupled to FE-SEM (BT = biotite, PL = plagioclase, PFL = K-feldspar, ZRC = zircon, EPD = epidote, Q = quartz and KLN = kaolinite).

resolved using digital autoradiography (Fuji Analyzer FLA 5100). In autoradiography an exposure time of 7 days and a resolution of 1016 dpi (pixel size: 25 μm) for the phosphor imaging plate (Fuji Imaging Plate, BAS-TR2025) was used. The spatial distribution of the C-14-PMMA was determined calibration series with known activities. When taking into account the beta correction factor (Siitari-Kauppi, 2002), the activities can be converted to a spatial porosity distribution using equation

$$\varepsilon_n = \frac{\rho_r/\rho_0}{1 + (\rho_r/\rho_0 - 1)A_n/A_0} \frac{A_n}{A_0} \tag{1}$$

where ε_n is porosity of a pixel n, ρ_r local density of the rock, ρ_0 density of C-14-PMMA, A_n the activity of pixel n and A_0 the activity of C-14-PMMA. Now the total connected porosity (ε_p) of the sample can be determined by equation

$$\varepsilon_p = \frac{\sum_{n=1}^{N} \varepsilon_n}{N} \tag{2}$$

where N is the total number of pixels. The spatial porosity distributions and total porosities were determined using Eqs. (1) and (2) and an in-house built MATLAB-script (MathWorks Inc., Natick, Massachusetts, USA) that applies the MATLAB Image Processing Toolbox.

Fractures were detected from autoradiographs using the algorithm depicted by Mazurier et al. (2016). The algorithm is based on mathematical morphology operators that are used to binarize and skeletonize the fractures and grain boundaries in the autoradiographs. The fracture densities [L^{-1}], average fracture porosities and fraction of fracture porosity from total porosity (the term fraction of fracture porosity used from here on) were determined using the skeletonized autoradiographs. The pixel size used (25 μm) of autoradiographs is lower than the maximal path of beta in silicates (~100 μm) and thus the fractions of fracture porosities were performed on a dilated skeleton. The fraction of fracture porosity represents here the part of the total connected porosity which belongs to fractures and it is not dependent on the aperture of fracture. Whereas the average fracture porosity is dependent on the aperture of fracture and applied pixel size (Sardini et al., 2014; Kuva et al., 2015a,b,c).

2.5. Chemical staining of minerals

The X-μCT can not distinguish the pores in the crystalline rock samples as their pore sizes are below the voxel size of the X-μCT (13.58 μm). Thus the 3-D mineral distribution does not contain any easily accessible information about the spatial porosity distribution of the rock. However, the spatial porosity distribution determined by the C-14-PMMA autoradiography can be combined with chemical staining of minerals and then mineral-specific porosities of the main minerals can be determined using the methods developed by (Sardini et al. 1999, 2006). Their methods were applied here for the chemical staining of minerals, superposition of stained rock surface with spatial porosity distribution and determination of mineral-specific porosities. After the chemical staining, the mica minerals are shown as blue, the plagioclase as white, the K-feldspar as yellow and the quartz remains unchanged. The stained surfaces were optically scanned in red-green-blue (RGB) 24 bit format using the same resolution (1016 dpi) as in the C-14-PMMA autoradiographs. This was followed by segmentation of stained images using their color histograms and superimposition of them with C-14-PMMA autoradiographs. For LTDE-SD-GRD1 and LTDE-SD-GRD2 samples the alteration rim was segmented from the less altered rock matrix by finding the interface between the two parts using the Carpet algorithm (Turpeinen et al., 2015). The algorithm was applied by using an in-house built plugin for ImageJ. Now the mineral-specific porosities and spatial porosity distributions can be determined separately for each main mineral using Eqs. (1) and (2). Note that mineral-specific porosities here contain all of the surface-connected porosity (intra- and inter-granular pores, and inter- and trans-granular fissures) associated with the mineral in question. Previously these methods have been successfully applied for determining the mineral-specific porosities of the main minerals in Grimsel granodiorite (Kelokaski et al., 2006) and altered Sievi tonalite (Voutilainen et al., 2012).

3. Results

3.1. Scanning electron microscopy

Examples of FE-SEM-EDS results for the alteration rim and for the less altered rock matrix of LTDE-SD-GDR are shown in Fig. 2 (upper panels) and the photographs of the analyzed rock surfaces are shown in
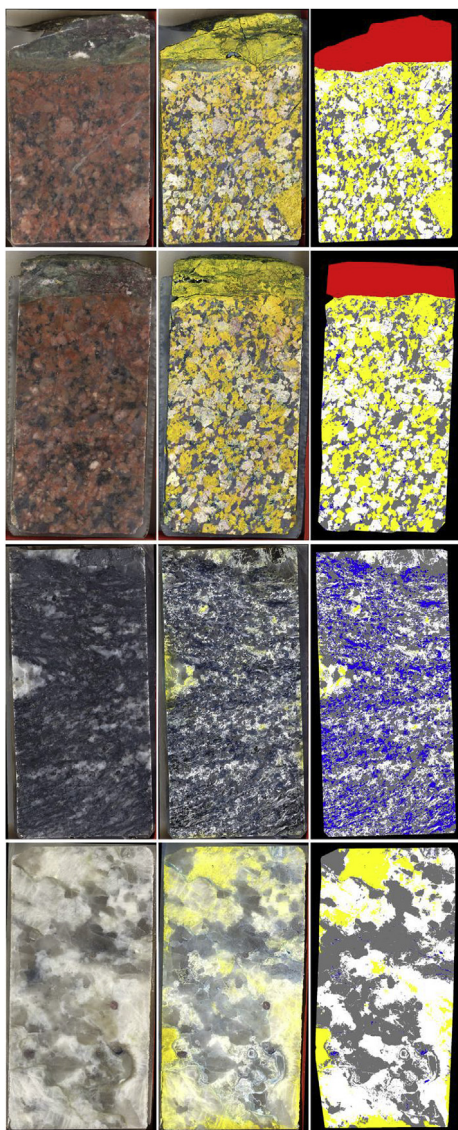
Fig. 3. The main minerals of LTDE-SD-GDR1 (1st row), LDTE-SD-GDR2 (2nd row), REPRO-VGN (3rd row) and REPRO-PGR (4th row) were stained chemically and segmented digitally. The photographs of original (left column) and chemically stained (middle column) of rock surface, and digitally segmented (right column) images are shown. In the stained and segmented images K-feldspar is yellow, plagioclase is white, mica minerals are blue, and quartz is gray. In the segmented images of LTDE-SD-GDR samples the alteration rim is shown as red. The width of the samples is 24 mm.

Fig. 3 (two uppermost rows). The FE-SEM-EDS study and visual inspection revealed that the rock matrix of the LTDE-SD-GDR sample was moderately hydrothermally altered and that the alteration rim consisted of coating, cataclasite and a greenish mylonitic part. The general alteration feature in the rock matrix is that plagioclase has been altered to secondary feldspars (albite and adularia), epidote and sericite. Furthermore, biotite has almost completely altered to chlorite. The rock matrix also contained thin vein-like features that were calcite and secondary K-feldspar. The thickness of these features varied from 20 μm to 70 μm. The amounts of micrometer scale pores was higher in these features and thus they are likely pronounced in the C-14-PMMA autoradiography. The coating of the alteration rim consists of secondary minerals such as chlorite, clay minerals (e.g. illite) and calcite. The fine-grained cataclasite part contains illite, K-feldspar, hematite, epidote, chlorite, quartz, large scattered crystals of calcite and rock matrix fragments (see Fig. 2). The fine-grained greenish mylonitic part consists

of more euhedral epidote than cataclasite part, K-feldspar, calcite, chlorite, quartz, and sulphides. In general, the micrometer scale intra-granular pores with the pore sizes of 0.5 μm–3 μm and 0.5 μm–5 μm were common in the rock matrix and alteration rim, respectively (see Fig. 2). The amount of inter-granular pores was not so high at this scale (magnification: × 1000) and the majority were in the fracture coating and in the vicinity of the alteration rim. The sizes ranged from 0.5 μm to 10 μm.

An example of FE-SEM-EDS results for REPRO-VGN is shown in Fig. 2 (lower left) and the photograph of the analyzed rock surface is shown in Fig. 3 (third row). The FE-SEM-EDS study revealed that the biotite grains are mostly unaltered having some grains with visible interlamellar pore openings filled with kaolinite (see Fig. 2) and some other grains with partly pinitized cordierite as inclusions. There were no traces of alteration found in plagioclase and K-feldspar grains. Furthermore, the quartz grains were found to be mostly intact. However, some of the grain boundaries contained kaolinite. The inter- and intra-granular pores ranged from 0.5 μm up to 10 μm in size (see Fig. 2). Most of the grain boundaries were found to be non-porous in applied scale (magnification: × 1000). The partly pinitized cordierite grains found are known to have high porosity and thus they are likely pronounced in the C-14-PMMA autoradiography (Kuva et al., 2018; Sammaljärvi et al., 2017).

An example of FE-SEM-EDS results for REPRO-PGR is shown in Fig. 2 (lower right) and the photograph of the analyzed rock surface is shown in Fig. 3 (fourth row). In general, the REPRO-PGR sample is very slightly altered (Sammaljärvi et al., 2017). The FE-SEM-EDS study revealed some secondary muscovite and illite in connection with perthitized K-feldspar grains as well as in some inter- and intra-granular pores in connection with quartz grains (see Fig. 2). The secondary mineral formation might be mostly a result of alteration of K-feldspar and plagioclase grains. Primary and secondary muscovite were the only mica minerals found in the sample and only in small abundances. The quartz grains were found to be mostly intact and no trace of alteration was found in them. The size of the inter- and intra-granular pores ranged from 0.5 μm up to 20 μm. Most of the grain boundaries were found to be porous in the applied scale (magnification: × 1000). Furthermore, the number of grain boundaries was higher than in the LTDE-SD-GDR and REPRO-VGN samples. Overall the results of all FE-SEM-EDS analyses were in agreement with the ones from previous studies performed for parallel samples from the sites (Widestrand et al., 2010b; Sammaljärvi et al., 2017).

3.2. Chemical staining of the minerals

The main minerals of all the samples were chemically stained in order to determine mineral-specific porosities when analyzing C-14-PMMA autoradiographs. The resulting images for rock surfaces before and after staining, and segmented surfaces are shown in Fig. 3. In general, the staining was complete and the stained minerals were successfully segmented using the methods introduced in Sec. 2.5. However, the staining was not successful for the alteration rim of LTDE-SD-GDR samples due to thorough hydrothermal alteration, the mylonitic nature and the fact that the applied chemicals did not function for clay minerals. Hence, the alteration rim was segmented from the rest of the samples as one mineral phase. After the staining process K-feldspar is shown as yellow, plagioclase as white, mica minerals (biotite, chlorite and muscovite) as blue and quartz is unchanged (grayish in Fig. 3). The mineral abundances determined according to the stained surfaces (see Table 2) are in fair agreement with the abundances determined previously for the parallel samples from the sites (see Table 1). The REPRO-VGN sample was from a section of the drill-core that had lower K-feldspar content than REPRO-VGN samples in general and thus abundance of it is minor compared with K-feldspar content in Table 1.

Previously it has been determined that the uncertainty of the method is less than 5% (Sardini et al., 1999). The uncertainties of the

Table 2
The mineral-specific and total connected porosities determined with the C-14-PMMA autoradiography for LTDE-SD-GDR1, LTDE-SD-GDR2, REPRO-VGN and REPRO-PGR. Abundances (%) of each mineral is given in parenthesis. Here mica minerals include biotite, chlorite and muscovite.

	GDR1 (%)	GDR2 (%)	VGN (%)	PGR (%)
K-feldspar	0.24 (32.6)	0.33 (31.8)	0.34 (0.6)	0.43 (10.1)
Plagioclase	0.32 (39.4)	0.44 (35.5)	0.39 (26.8)	0.33 (47.1)
Quartz	0.33 (26.6)	0.45 (31.3)	0.22 (55.0)	0.36 (42.4)
Mica minerals	1.0 (1.4)	1.1 (1.4)	0.17 (17.6)	1.9 (0.4)
Alteration rim	2.6 (17.8)	2.9 (11.9)	–	–
Matrix	0.31 (82.2)	0.42 (88.1)	–	–
Total	0.71 (100.0)	0.72 (100.0)	0.26 (100.0)	0.36 (100.0)

staining are related to grain size of the samples, accessory minerals and alteration. If the typical grain size is near the resolution of the scanned image, it might be difficult to determine reliably the mineral phase of the pixel as the signal might be coming from multiple minerals. In this work the resolution of the scanned images was selected according to the resolution of the C-14-PMMA autoradiography. Moreover, in the C-14-PMMA autoradiography it is not meaningful to use a resolution below 20 μm which is roughly the mean range of β-particles emitted by C-14 atoms. The samples investigated in this work had grain sizes well above 20 μm and thus the comparison of segmented mineral distributions and spatial porosity distributions are feasible. Furthermore, the abundance of accessory minerals were about 3% for LTDE-SD-GDR, 10% for REPRO VGN and 0.7% for REPRO-PGR (Widestrand et al., 2010b; Sammaljärvi et al., 2017). In the REPRO-VGN sample the amounts of partly pinitized cordierite and sillimanite are noteworthy and the issue is discussed thoroughly in the following section. The alteration, on the other hand, is minor in the REPRO-VGN and REPRO-PGR samples and thus the effect of it can be considered negligible for the staining process. In LTDE-SD-GDR the biotite has altered mostly to chlorite, and plagioclase has been altered mostly to albite and adularia. Fortunately all plagioclases (including albite) are colored as white in the hydrofluoric acid treatment. The adularia is a variant of K-feldspar which is colored yellow in the sodium cobaltnitride treatment.

3.3. C-14-PMMA autoradiography

The total connected porosities and mineral-specific porosities were determined from C-14-PMMA autoradiographs (see Fig. 4 and Table 2). Furthermore, the average fracture porosities and fraction of fracture porosities were determined from the C-14-PMMA autoradiographs and the fracture densities from C-14-PMMA autoradiographs and X-μCT images (see Table 3).

For LTDE-SD-GDR samples, C-14-PMMA autoradiographs show a more porous alteration rim than rest of the rock matrix. Both parts show a heterogeneous spatial distribution of porosity. The alteration rims had total porosities of 2.6% (LTDE-SD-GDR1) and 2.9% (LTDE-SD-GDR2) and the cataclasite part has higher porosity than the mylonitic part, which has very low porosity. The porosity of the rock matrix consists of both grain boundary porosity and intra-granular porosity. The grain boundary pores are seen as thin vein-like features and intra-granular porosity is seen as more-or-less even gray areas in the autoradiographs. The total connected porosity of the rock matrix was 0.31% (LTDE-SD-GDR1) and 0.42% (LTDE-SD-GDR2). Furthermore, there are fracture-like features crossing through both of the LTDE-SD-GDR samples. These features arise from the calcite and secondary K-feldspar filled fractures that were identified using FE-SEM-EDS. The average fracture porosities were 1.4% (LTDE-SD-GDR1) and 2.0% (LTDE-SD-GDR2) in the rock matrix and 13.9% (LTDE-SD-GDR1) and 5.8% (LTDE-SD-GDR2) in the alteration rim that indicates opening of fractures in this zone. The fractions of fracture porosities were 0.20 (LTDE-SD-GDR1) and 0.17 (LTDE-SD-GDR2) in the matrix and 0.20 (LTDE-SD-GDR1) and 0.14

(LTDE-SD-GDR2) the alteration rim. These values indicate that majority of the porosity lies within the porous minerals. As expected, fracture density in the rock matrix is similar in two LTDE-SD-GDR samples (9.8 and 10.7 cm^{-1}). In the alteration zone, the variability of fracture density is higher (10 and 5.9 cm^{-1}), but are in fair agreement with the fracture density of the matrix.

The C-14-PMMA autoradiograph of REPRO-VGN in Fig. 4 shows a slightly orientated spatial distribution of porosity, only few vein-like features, and few scattered spots with high porosity. The orientation in the autoradiograph arises from schistosity of the main minerals that can be seen from the photograph of the rock surface (see Fig. 3). The total porosity of the REPRO-VGN sample was 0.26%, consisting mostly of intra-granular porosity as the number of micrometer scale grain boundary pores is minor. The highly porous grains in the autoradiograph originate from the partly pinitized cordierites (Sammaljärvi et al., 2017; Kuva et al., 2018) that were identified using FE-SEM-EDS. The abundance of the partly pinitized cordierite grains is 1.0% which is lower than generally observed in VGN samples from the REPRO site (Sammaljärvi et al., 2017). Average fracture porosity was 0.71% that indicate relatively low apertures of fractures in this sample. The fraction of fracture porosity is 0.28 that indicates that majority of the porosity lies within the porous minerals. Fracture density in the rock matrix (9.3 cm^{-1}) is similar than what was found for LTDE-SD-GDR samples.

The REPRO-PGR sample has a spatial distribution of porosity that consists mostly of grain boundary pores (including inter-granular and trans-granular fissures) but also some mineral-specific porosity (see Fig. 4). Furthermore, some of the mineral grains are non-porous as their gray value is at the same level as the background. The grain boundaries are larger in the C-14-PMMA autoradiograph than what was observed with FE-SEM-EDS. The enlarging can be explained partly by the range of β-particles emitted by C-14 atoms and that the grain boundaries may be tilted with respect to the surface of the sample (Kuva et al., 2015b). However, some of the features are thicker than can be assumed from the FE-SEM-EDS results and thus it can be concluded that there are areas with increased porosity near grain boundaries, or thicker inter-granular and trans-granular fissures with filling (e.g. illite or muscovite that were found using FE-SEM-EDS) in them. The average fracture porosity of PGR sample is 1.3% that indicates similar average apertures than in LTDE-SD-GDR samples. Total fracture porosity is 0.54 that is larger than for LTDE-GDR and REPRO-VGN and implies that more than half of the porosity lies within the fractures and grain boundaries. Fracture density in the rock matrix (17.8 cm^{-1}) is clearly higher than the two previous studied samples.

The mineral-specific porosities of main minerals were determined by superimposing segmented mineral images with spatial porosity distributions (see Fig. 3) and by determining the total connected porosity within the area of each main mineral. The mean values for the mineral-specific porosities are given in Table 2 and porosity distributions within the area of each main mineral in Fig. 5. Furthermore, the porosity distributions of whole samples are given for comparison in Fig. 5. The main peak of the porosity distribution for the alteration rim of LTDE-SD-GDR samples is roughly at the same location as in the porosity distribution of the rock matrix. However, the porosity distribution of the alteration rim has more pixels with porosities over 2% which makes its total porosity larger than that of the rock matrix. The mica minerals (mostly chlorite according to the FE-SEM-EDS results) have the highest and the K-feldspar the lowest mineral-specific porosity. There are no large differences in shapes of the porosity distributions of the main minerals and the porosity is distributed relatively similarly in all main minerals. This in agreement with FE-SEM-EDS study where all the main minerals were found to contain intra-granular pores with aperture below resolution of the C-14-PMMA autoradiography. Furthermore, with high porosities the porosity distribution decreases almost linearly on a log-log scale. This is not the case for REPRO-VGN and REPRO-PGR samples. Alteration of biotite to chlorite
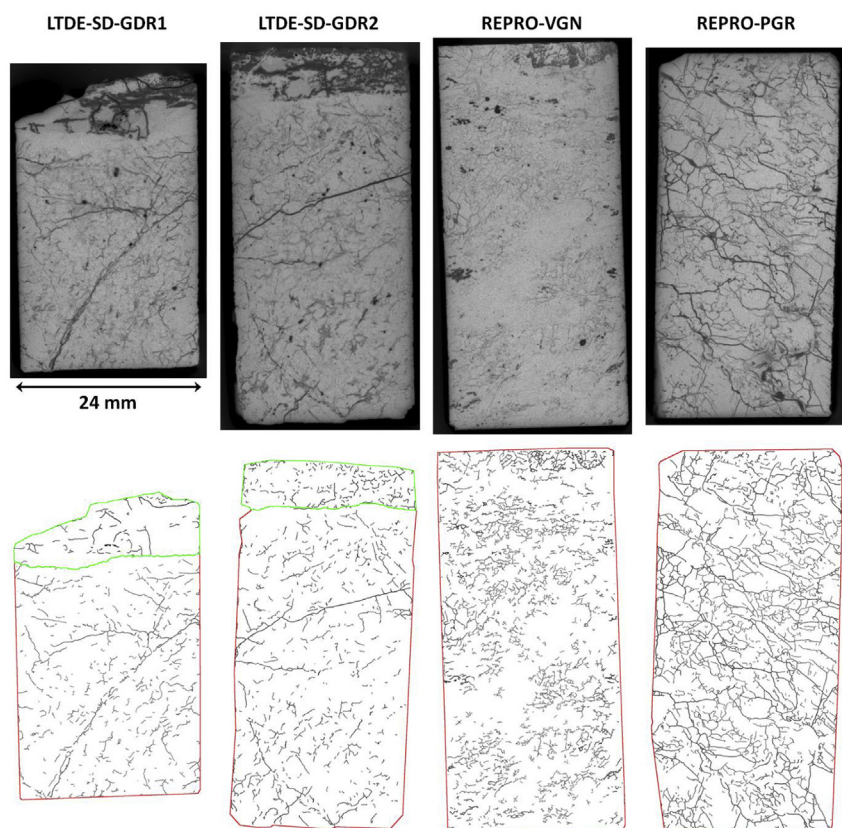
LTDE-SD-GDR1   LTDE-SD-GDR2   REPRO-VGN   REPRO-PGR

24 mm

Fig. 4. The C-14-PMMA autoradiographs (upper panels) and segmented fractures and grain boundaries (lower panels) show the spatial porosity distribution of LTDE-SD-GDR1, LTDE-SD-GDR2, REPRO-VGN and REPRO-PGR samples (from left to right). In the C-14-PMMA autoradiographs dark shades of gray correspond to high porosity and light shades of gray to low porosity. In segmented fracture images red boxes indicate the analyzed area for the rock matrix and green boxes the analyzed areas for alteration rims. (For interpretation of the references to color in this figure legend, the reader is referred to the Web version of this article.)

Table 3

Average fracture porosities and fraction of fracture porosities determined from C-14-PMMA autoradiographs and fracture densities determined from C-14-PMMA autoradiographs and X-μCT images. The results are given for LTDE-SD-GDR1, LTDE-SD-GDR2, REPRO-VGN and REPRO-PGR. A separate values are given for alteration rims of LTDE-SD-GDR1 and LTDE-SD-GDR2.

		GDR1	GRD2	VGN	PGR
Average fracture porosity – matrix (%)		1.4	2.0	0.71	1.3
Average fracture porosity – alteration rim (%)		13.9	5.8	–	–
Fraction of fracture porosity – matrix (−)		0.20	0.17	0.28	0.54
Fraction of fracture porosity – alteration rim (−)		0.20	0.14	–	–
C-14-PMMA autoradiography	Fracture density – matrix (1/cm)	10.0	5.9	9.3	17.8
	Fracture density – alteration rim (1/cm)	9.8	10.7	–	–
X-μCT	Fracture density – matrix (1/cm)	49.6	–	40.6	14.6
	Fracture density – alteration rim (1/cm)	7.3	–	–	–

has caused a slight increase in its porosity. However, it has not increased the total connected porosity considerably with respect to unaltered samples from the area (Widestrand et al., 2010b) because the abundance of mica minerals is only around 1.6% on the analyzed rock surfaces.

In REPRO-VGN the porosity distributions for the different main minerals are similar (see Fig. 5) and the average mineral-specific porosities are closer to each other than for the LTDE-SD-GDR samples. Differences in distributions can be seen on the high porosity end of the distributions that are affected by the partly pinitized cordierite grains. These grains can not be separated by the chemical staining and thus the results are slightly distorted. Fortunately the analyzed surface has less cordierite grains than generally in VGN samples from the REPRO site (Sammaljärvi et al., 2017). The analysis showed that according to chemical staining 55% of the porous grains belong to plagioclase areas,

40% to quartz areas, 5% to mica mineral areas, and less than 1% to K-feldspar areas. In log-log scale the partly pinitized cordierite grains cause a small shoulder to the porosity distributions of plagioclase and quartz. However, in the porosity distribution of the mica minerals such a shoulder can not be seen. Hence, the mineral-specific porosities of plagioclase and quartz may be slightly overestimated in this case. In general, the total connected porosity is slightly lower than typically measured for VGN samples from the REPRO site (Kuva et al., 2015c; Sammaljärvi et al., 2017). This can be explained by the low abundance of partly pinitized cordierites and the heterogeneous nature of the samples.

The shapes of porosity distributions for plagioclase, quartz and K-feldspar of the REPRO-PGR sample are somewhat similar (see Fig. 5). These distributions consist of a main peak arising from intra-granular porosity and a small shoulder from the grain boundary porosity including inter- and trans-granular fissures. The mode values of the distributions differ slightly which are reflected in the mean values of mineral-specific porosities given in Table 2. The abundance of mica minerals (consisting of primary and secondary muscovite according to FE-SEM-EDS results) is only 0.35%. It has, however, the highest mineral-specific porosity. In general, the total connected porosity is at the lower side of the porosities determined previously for PGR samples from the REPRO site (Kuva et al., 2015c; Sammaljärvi et al., 2017).

3.4. X-ray micro computed tomography

The LTDE-SD-GDR1, REPRO-VGN and REPRO-PGR samples were scanned using the X-μCT and representative cross-sections before image processing are shown in Fig. 6. The reconstructed and denoised 3-D images were further processed by segmenting the different mineral phases according to their X-ray attenuation coefficient and the grain distribution of each mineral phase. Examples of segmented mineral phases and grain distributions are shown in Fig. 6. Unfortunately some of the main minerals could not be segmented from each other due to
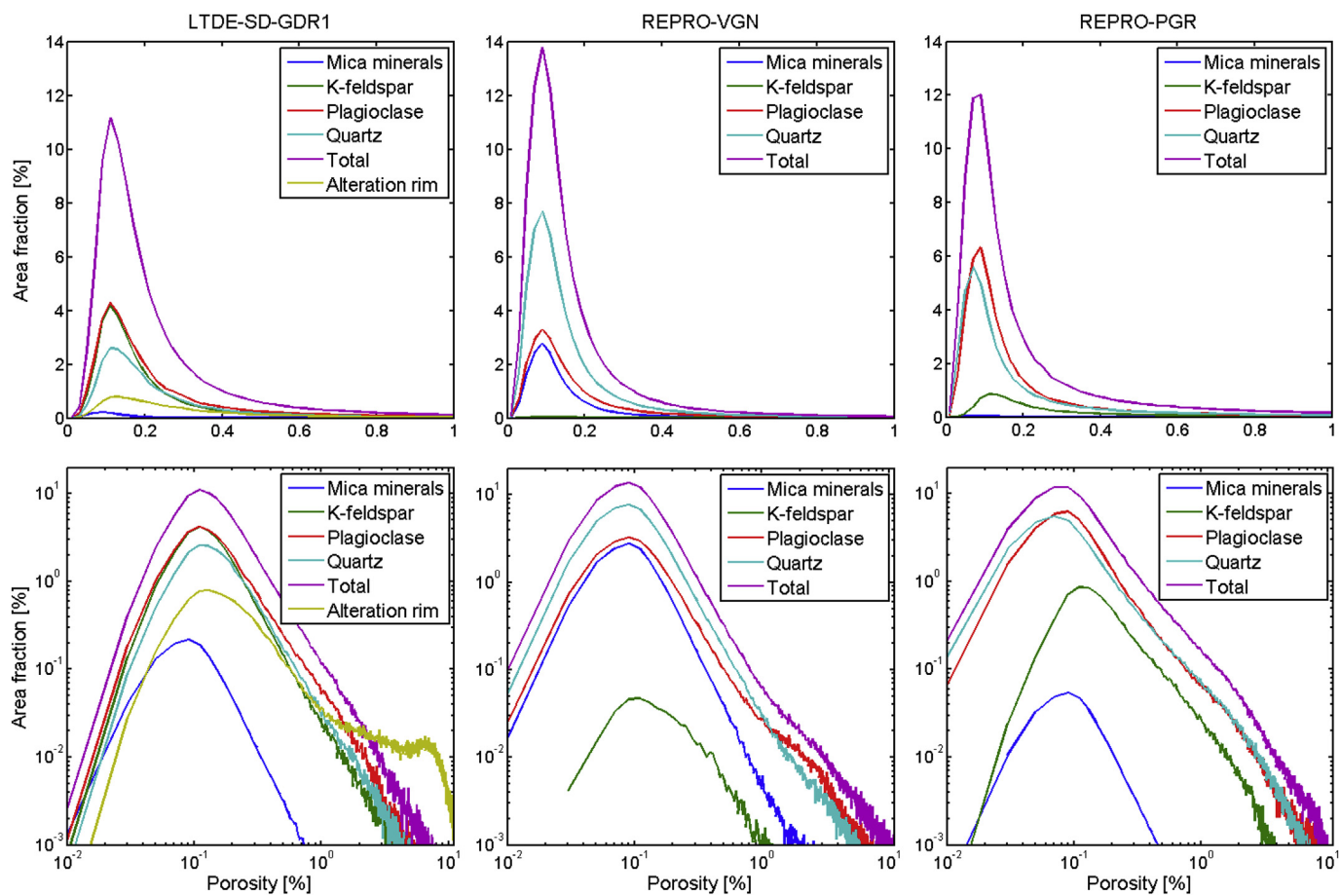
Fig. 5. Porosity histograms of LTDE-SD-GDR1 (left column), REPRO-VGN (middle column), and REPRO-PGR (right column) samples in linear (upper row) and log-log (lower row) scale. The histograms were determined using 20 μm resolution C-14-PMMA autoradiographs (the original and segmented) and a binning of 0.02%.
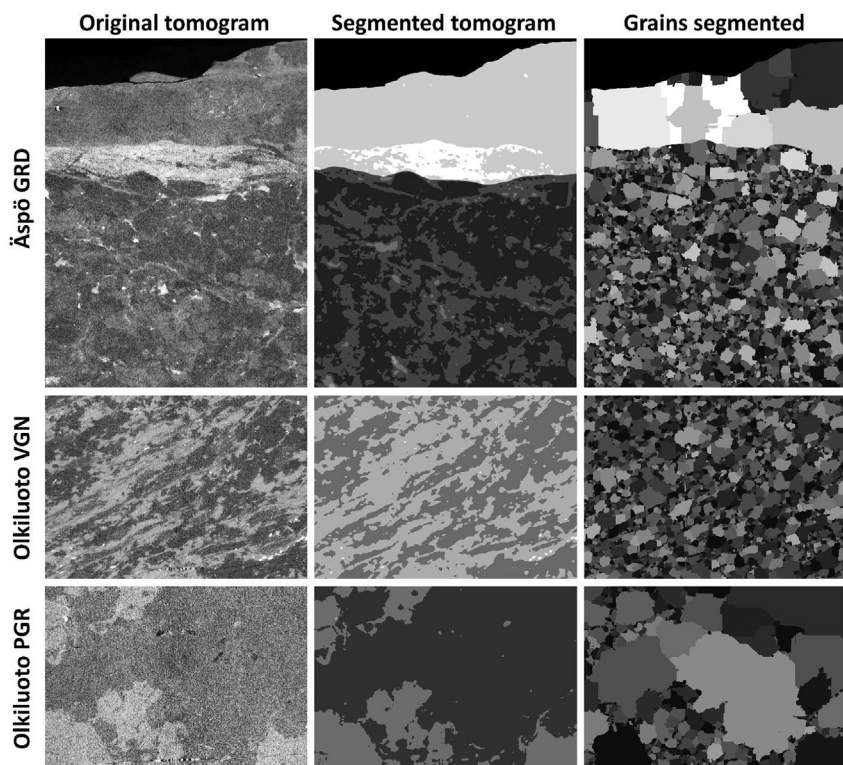

Fig. 6. The cross sections of the original tomographic image (left column), and tomographic images with segmented mineral phases (middle column) and grains (right column). The cross sections for LTDE-SD-GDR1 (upper row), REPRO-VGN (middle row) and REPRO-PGR (lower row) are shown. The mineral phases were segmented based on the gray values in the original image and grains were segmented using the watershed algorithm. The content of different mineral phases and the gray values used in the middle column are given in Table 3. In the right column each segmented grain is given a random gray value.
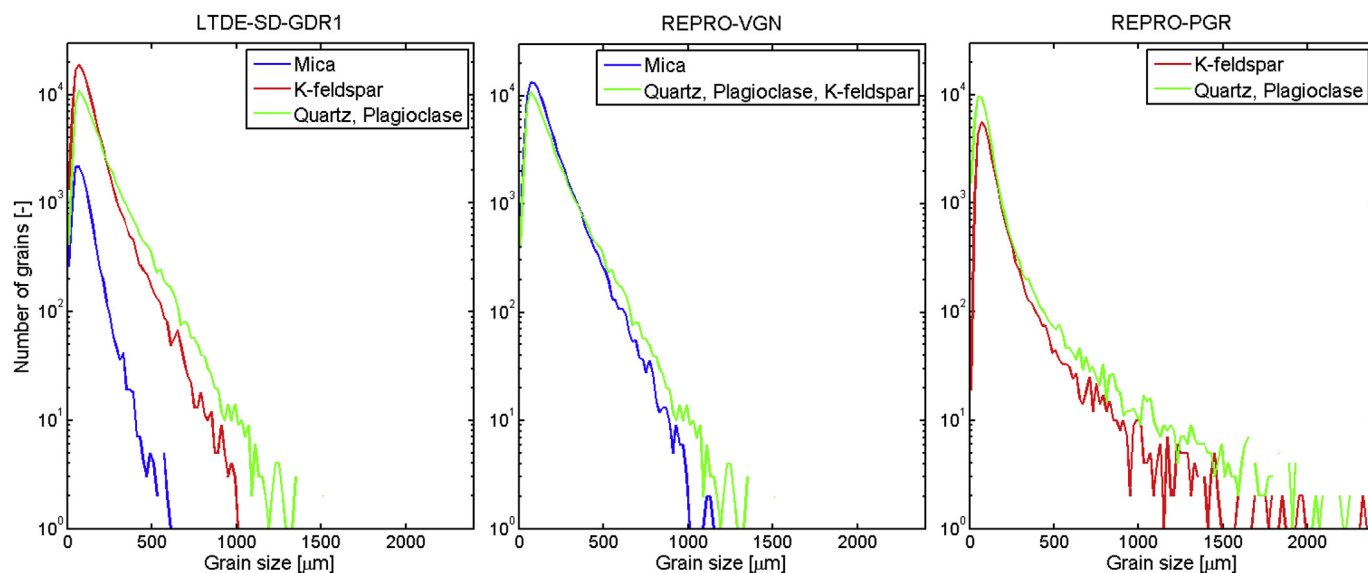
Fig. 7. Grain size distributions of the LTDE-SD-GDR1 (left column), REPRO-VGN (middle column), and REPRO-PGR (right column) samples. The distributions were determined from tomographic images with grains segmented, and the distributions are determined using 20 μm bin size.

similar X-ray attenuation coefficients and thus they are linked to one mixed mineral phase. This was the case for plagioclase, quartz and K-feldspar in the REPRO-VGN sample and plagioclase and quartz in the LTDE-SD-GDR1 and REPRO-PGR samples. Grain size distributions, shown in Fig. 7, were determined for each mineral and mineral phase from grain distribution images. The spatial grain distributions were constructed virtually using the watershed algorithm. When using such method the grains are not defined like typically in crystallography as the watershed algorithm involves known issues of over-segmentation (Chen et al., 2004). However, as the grains contain trans-granular fissures the constructed spatial grain distributions can be better applied in the reactive transport modeling. Furthermore, the segmentation of the grains enables a division of the mixed mineral phases to the main minerals that the phase consists. The results of division are given below in Sec. 4.

In the rock matrix of the LTDE-SD-GDR1 sample, four mineral phases were segmented from the tomographic image: the mixed mineral phase containing plagioclase and quartz, K-feldspar, mica minerals (mostly chlorite), and dense accessory minerals. The number of the mineral grains in K-feldspar and mixed mineral phases are similar (see Fig. 7). The K-feldspar phase has slightly more small mineral grains (around 100 μm) than the mixed mineral phase and the mixed mineral phase has more larger grains (> 500 μm) than the K-feldspar phase. The mica mineral phase consists mainly of small mineral grains (< 200 μm). In the alteration rim the cataclasite and greenish mylonitic parts had different X-ray attenuation coefficients and thus they could be segmented from each other. The grain distribution of the alteration rim is under-segmented due to a large continuous phase of the cataclasite part whereas the mylonitic part is known to have extremely small grain size. Thus their grain size distributions are not presented. In the rock matrix of LTDE-SD-GDR1, the virtual fracture densities determined from X-μCT images are very dense (49.6 cm^{-1}) compared to the densities obtained from C-14-PMMA autoradiography (10 cm^{-1}). This difference arise from the over-segmentation of the watershed algorithm. This could, however, be seen has an advantage as discussed below in Sec 4. In the alteration rim, however, fracture densities are similar from one method to the other (see Table 3).

The mica minerals, mixed mineral phase containing mainly quartz and plagioclase and some K-feldspar, and dense accessory minerals were segmented from the tomographic image of the REPRO-VGN sample (see Fig. 6). In a study by Kuva et al. (2018), it was shown that the X-ray attenuation of the partly pinitized cordierite grains overlap

with the quartz and feldspar grains. Thus the mixed mineral phase contains here also these cordierite grains. The tomographic images show clearly the foliated structure of the REPRO-VGN sample that is typical for this type of samples. The number of the mineral grains in mica mineral and mixed mineral phases are similar (see Fig. 7). The mixed mineral phase has slightly more larger mineral grains (> 500 μm) than the mica mineral phase. Similarly to what was obtained for the LTDE-SD-GDR, the virtual fracture densities determined from X-μCT images are denser (40.6 cm^{-1}) than the densities obtained from C-14-PMMA autoradiography (9.3 cm^{-1}). This difference arises from the over-segmentation of the watershed algorithm.

The K-feldspar, mixed mineral phase containing quartz and plagioclase, and dense accessory mineral phases were segmented from the tomographic image of the REPRO-PGR sample (see Fig. 6). The sample consists mainly of the mixed mineral phase (69.6%) and K-feldspar (30.4%). The mica minerals could not be found in the tomographic image due to the small grain size of muscovite grains and they are mostly disseminated in the quartz and feldspar phases. However, some of the muscovite grains may be mixed in the phase of dense accessory minerals. The grain size distributions of the REPRO-PGR sample show a non-linear decrease in the log-log scale with large grain sizes whereas the distributions of LTEDE-SD-GDR1 and REPRO-VGN samples show a linear behavior at the same range. The number of large grains (> 1000 μm) is significantly higher in the grain size distributions of REPRO-PGR sample than in the other samples. This is in agreement with the fact that REPRO-PGR has a larger grain size than the other samples, and can be seen also by comparing the tomographic images with grains segmented (see Fig. 6). The intra-granular pores or trans-granular fissures observed in the REPRO-PGR sample using the C-14-PMMA autoradiography could not be observed using the X-μCT, which strengthens the observation that most of these features are below the 10 μm of are filled by alteration products. However, these features are without a doubt important for the transport of solutes in REPRO-PGR and they should be taken into account when performing the reactive transport modeling. It is very informative to observe that fracture densities obtained from C-14-PMMA autoradiography and X-μCT images are in good agreement (17.8 and 14.6 cm-1, respectively, see Table 3). This is obviously due to the coarse grain size of REPRO-PGR. The watershed segmentation of X-μCT provides less new intra-mineral grain boundaries than for a fined grained matrix. Furthermore, in REPRO-PGR the grains are granular where as in LTDE-SD-GDR and REPRO-VGN there is orientated minerals that are more prone to over-

Table 4
The porosities of different mineral phases in LTDE-SD-GRD, REPRO-VGN and REPRO-PGR and gray value used for each mineral phase in Fig. 6. The porosities for mineral phases containing multiple main minerals have been determined using the real mineral abundances and their porosities given in Table 2. The abundances of each mineral phase in the tomographic images are also given.
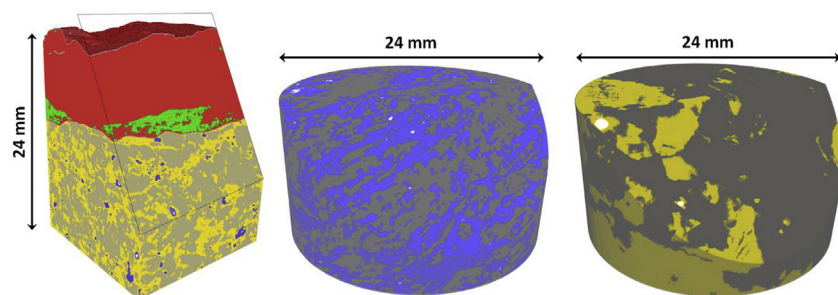
Sample	Mineral phase	Abundance (%)	Gray value	Porosity (%)
LTDE-SD-GRD1	Quartz, Plagioclase	(56.1)	42	0.39
	K-feldspar	(42.2)	85	0.29
	Mica minerals	(1.6)	127	1.1
	Accessory	(0.07)	171	-
	Alteration rim	(34.6)	212 and 255	2.7
REPRO-VGN	Quartz, Plagioclase, K-feldspar	(57.5)	124	0.28
	Mica minerals	(42.4)	186	0.17
	Accessory	(0.08)	255	-
REPRO-PGR	Quartz, Plagioclase	(69.6)	63	0.34
	K-feldspars	(30.4)	127	0.43
	Accessory	(0.06)	255	-

Fig. 9. The spatial distributions minerals of LTDE-SD-GDR1 (left), REPRO-VGN (middle) and REPRO-PGR (right). The result of grain segmentation and arbitrary division of mixed mineral phases show the partly artificial spatial distribution of mica minerals (blue), K-feldspar (yellow), quartz (gray), plagioclase (white) and alteration rim (red).
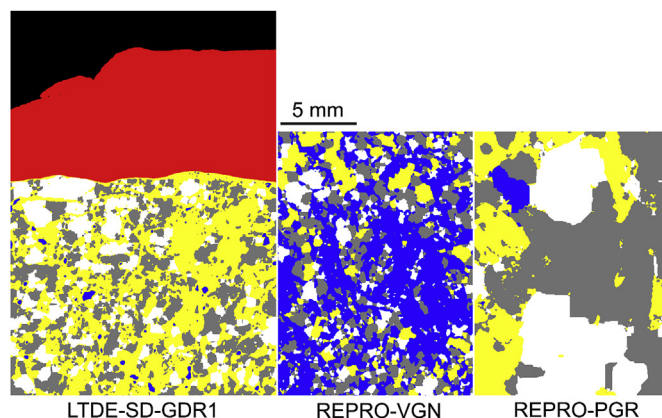
segmentation than the granular ones.

4. Discussion and summary

The mineral-specific porosities determined using the C-14-PMMA autoradiography and chemical staining of minerals can be linked to segmented tomographic images. The porosities given in Table 4 for the mixed mineral phases are determined by taking into account the porosity and the abundance of each main mineral in the phase. After this, the 3-D tomographic images shown in Fig. 8 can be considered as the spatial porosity and mineral distribution. In Fig. 8, the mica minerals are shown as blue, K-feldspar as yellow, mixed mineral phases as gray and dense accessory minerals as white.

The mixed mineral phases in Fig. 8 were further divided to the main minerals that the phase contains. This was done by dividing separated grains (see Fig. 6, right column) belonging to the mixed mineral phase arbitrarily to its minerals (LTDE-SD-GDR1 and REPRO-PGR (right): quartz and plagioclase; REPRO-VGN: K-feldspar, plagioclase and quartz.). The real abundances given in Table 1 were applied when performing the division. The resulting 3-D mineral distributions, shown in Fig. 9, are similar with the ones determined using chemical staining of the main minerals (see 3, right column). However, in a few occasions the over segmentation caused by the watershed algorithm can be observed. Even though it is known that the grain segmentation is not completely realistic, this can be considered as major step towards increased realism for representing the heterogeneous mineral distribution of crystalline rock in 3-D. Furthermore, the similarity of spatial mineral distributions determined using chemical staining of minerals and segmentation of tomographic images builds confidence on the results. When using this kind of spatial mineral distribution in the reactive transport modeling, porosities given in Table 2 and mineral specific

geochemical reactions can be applied. In general, the representation of the spatial porosity distribution in 3-D could be further developed by generating statistically porosity distributions given in Fig. 5 for each main mineral. In theory, it is possible to generate the spatial porosity distributions in 3-D so that they would be similar to the spatial porosity distributions determined using the C-14-PMMA autoradiography (see Fig. 4).

For a full understanding about reactive transport in crystalline rocks, one main goal of this study has been to provide realistic 3-D modeling grids which are generated by combining the data produced using X-μCT and C-14-PMMA autoradiography. In these grids, special attention has to be paid in order to include fractures, because (1) they represent a reality, observed at all scales and (2) they constitute fast transport pathways through the rock for solutes (Sardini et al., 2007). It is important to note that, for the studied rocks, the fraction of fracture porosity represents from 0.17 to 0.54 fraction of the total connected porosity. In the present study, a conceptual model integrating fractures and mineral specific porosities is presented. Fractures are characterized by C-14-PMMA autoradiography in terms of the fracture density, average fracture porosity and fraction of fracture porosity. Unfortunately, C-14-PMMA autoradiography offers only 2-D information and the fractures have to be taken into account indirectly by applying image processing algorithms in 3-D X-μCT images.

Transposition of fracture parameters obtained from C-14-PMMA autoradiography to X-μCT images is not a trivial step in the proposed methodology. The X-μCT does not detect the fractures in the crystalline rock matrices due to their low apertures compared with employed voxel size and thus the watershed algorithm has been employed to create the virtual fracture network. This process is now discussed looking the obtained fracture densities (Table 3). Two cases can be discerned:

(1) Fracture densities are very similar from C-14-PMMA

Fig. 8. The segmented tomographic images show spatial distribution of mica minerals (blue), K-feldspar (yellow), mineral phase (gray) that contain multiple minerals, alteration rim (red and green), and dense accessory minerals (white). In the LTDE-SD-GDR1 (left) and REPRO-PGR (right) samples the mineral phases contain mainly quartz and plagioclase, and in the REPRO-VGN sample (middle) K-feldspar, plagioclase and quartz.

autoradiography than from X-µCT. This is the case for the alteration rim of LTDE-SD-GDR and REPRO-PGR that has coarser grain size.

(2) Fracture densities are higher using X-µCT due to the over-segmentation issues when applied to fine grained matrices. To compensate the over-segmentation, a simple solution would be to select randomly some fractures among the whole fractures set available from watershed segmentation, in order to obtain the same density as C-14-PMMA results. One possible and feasible refinement of that technique would be also to condition the obtained densities according to the minerals that are near the fractures.

If fracture densities are now imposed from C-14-PMMA autoradiography, the next important step would be to set the fracture porosities according to average fracture porosities in the X-µCT images. Note that the porosity distributions can also be used instead of the average values. However, care should be taken when transposing these porosity values since the pixel and voxel sizes should be similar. If not, a new porosity value should be estimated for fractures in the X-µCT images. This could be done for example using an approach suggested in recent studies by Sardini et al. (2014) and Kuva et al. (2015a,b,c).

The resulting representations of the crystalline rock samples can be applied in the reactive transport modeling using various methods (e.g. (Voutilainen et al., 2013; Blunt et al., 2013; Trinchero et al., 2017; Voutilainen et al., 2017; Park and Ji, 2018)). In the modeling the parameters for geochemical reactions can be defined taking into account the reacting compound and the mineral in the vicinity of the compound. It is possible to model the reactive transport inside the porous minerals and on the grain boundaries formed by the determined grain distribution. Furthermore, the results of FE-SEM-EDS can be applied when adjusting parameters for mineral specific geochemical reactions and for apertures between the mineral grains. In some cases, however, further experimental studies, such as (Muuri et al. 2016, 2017), may be needed. In previous studies, approximations have been made regarding the chemical reactions and, typically, only one reactive grain type has been used. This is not the case in real crystalline rock samples as Muuri et al. (2016, 2017) have shown in their studies. In this work, we have separated the mixed mineral phases and by applying this kind of approach for sample characterization the different reactive properties of the main minerals can be taken into account in the reactive transport modeling. Adjusting the apertures between the mineral grains is particularly important in the case of REPRO-PGR where the continuous network of inter-granular pores and trans-granular fissures were observed. These features form preferential pathways to solute transport and their effect needs to be carefully estimated for the reactive transport modeling.

5. Conclusions

The spatial porosity and mineral distributions of three type of crystalline rock samples from Äspö HRL and ONKALO, Olkiluoto, were successfully characterized using the X-µCT, C-14-PMMA autoradiography and FE-SEM-EDS. The combination of these methods was found to be a powerful tool for the characterization of the spatial porosity and mineral distribution of crystalline rock samples. It was shown that the limitations of a single method can be overcome by using multiple methods with different specifications. It was demonstrated that methods can be used to characterize crystalline rock samples of a various kind and applied to separate the hydrothermal alteration rim and from the less altered rock matrix. Furthermore, it was shown how the realism of the constructed spatial distributions can be increased by analyzing the density of fractures and porosities linked to them and by the virtual construction heterogeneous mineral distributions of minerals that cannot be separated by X-µCT. In addition, it was thoroughly discussed how these constructed spatial distributions could be applied further in the reactive transport modeling.

The combination of different analysis methods that cover a wide range of length scales can be used to infer novel structural information about crystalline rock. This kind of characterization has not been performed as extensively previously. It is evident that the methods employed can be further developed by: (i) constructing a more accurate porosity distribution of the sample in 3-D by using a 2-D spatial porosity distribution including grain boundary pores from the C-14-PMMA autoradiography and appropriate image processing algorithms, and (ii) developing methods and image processing tools related to the X-µCT so that minerals with similar X-ray attenuation coefficients could be segmented accurately. However, the partly virtually constructed heterogeneous mineral distributions linked to mineral-specific porosities can already be used to evaluate the effect of heterogeneities in LTDE-SD and REPRO experiments and possibly to explain the anomalous results of in situ experiments. More generally, the characterized distributions of the LTDE-SD-GDR samples can be applied to evaluate the interaction between fracture groundwater and pore water. In safety evaluations of spent nuclear fuel disposal, one of the key points is the interaction of radionuclides transported by mobile water in fractures with the immobile water and mineral surfaces of the rock matrix. This issue can also be further studied in the centimeter scale samples with micrometer scale heterogeneities by applying the results of this study and an appropriate modeling tool that is capable of modeling the reactive transport of radionuclides in fracture flow and their interaction with different minerals.

Acknowledgements

Appendix A. Supplementary data

Supplementary data to this article can be found online at https://doi.org/10.1016/j.apgeochem.2018.12.024.

References

Anselmetti, F.S., Luthi, S., Eberli, G.P., 1998. Quantitative characterization of carbonate pore systems by digital image analysis. AAPG Bull. 82, 1815–1836. https://doi.org/10.7892/boris.87075.

Blunt, M.J., Bijeljic, B., Dong, H., Gharbi, O., Iglauer, S., Mostaghimi, P., Paluszny, A., Pentland, C., 2013. Pore-scale imaging and modelling. Adv. Water Resour. 51, 197–216. https://doi.org/10.1016/j.advwatres.2012.03.003.

Bugani, S., Camaiti, M., Morselli, L., Van de Casteele, E., Janssens, K., 2007. Investigation on porosity changes of Lecce stone due to conservation treatments by means of X-ray nano- and improved micro-computed tomography: preliminary results. X Ray Spectrom. 36, 316–320. https://doi.org/10.1002/xrs.976.

Chen, Q., Yang, X., Petriu, E.M., 2004. Watershed segmentation for binary images with different distance transforms. In: Proceedings of 3rd IEEE International Workshop on Haptic, Audio and Visual Environments and Their Applications. IEEE, Piscataway, pp. 111–116. https://doi.org/10.1109/HAVE.2004.1391891.

Cnudde, V., Boone, M., 2013. High-resolution X-ray computed tomography in geosciences: a review of the current technology and applications. Earth Sci. Rev. 123, 1–17. https://doi.org/10.1016/j.earscirev.2013.04.003.

Denison, C., Carlson, W.D., 1997. Three-dimensional quantitative textural analysis of metamorphic rocks using high-resolution computed X-ray tomography: Part II. Application to natural samples. J. Metamorph. Geol. 15, 45–57. https://doi.org/10.1111/j.1525-1314.1997.00007.x.

Feldkamp, L.A., Davis, L., Kress, J., 1984. Practical cone-beam algorithm. J. Opt. Soc. Am. A 1, 612–619. https://doi.org/10.1364/JOSAA.1.000612.

Fusseis, F., Xiao, X., Schrank, C., De Carlo, F., 2014. A brief guide to synchrotron radiation-based microtomography in (structural) geology and rock mechanics. J. Struct. Geol. 65, 1–16. https://doi.org/10.1016/j.jsg.2014.02.005.

Gonzalez, R., Woods, R., 2002. Digital Image Processing. Prentice-Hall, New Jersey.

Hellmuth, K.-H., Siitari-Kauppi, M., Lindberg, A., 1993. Study of porosity and migration pathways in crystalline rock by impregnation with 14Cpolymethylmethacrylate. J. Contam. Hydrol. 13, 403–418. https://doi.org/10.1016/0169-7722(93)90073-2.

Hellmuth, K.-H., Lukkarinen, S., Siitari-Kauppi, M., 1994. Rock matrix studies with carbon-14-polymethylmethacrylate (PMMA): method development and applications. Isot. Environ. Health S. 30, 47–60. https://doi.org/10.1080/00211919408046712.

Ikonen, J., Sammaljärvi, J., Siitari-Kauppi, M., Voutilainen, M., Lindberg, A., Kuva, J., Timonen, J., 2015. Investigation of Rock Matrix Retention Properties – Supporting Laboratory Studies I: Mineralogy, Porosity, and Pore Structure, Working Report 2014-68. Posiva Oy, Olkiluoto, Finland.

Iraola, A., Trinchero, P., Voutilainen, M., Gylling, B., Selroos, J.-O., Molinero, J., Svensson, U., Bosbach, D., Deissmann, G., 2017. Microtomography based inter-granular network for the simulation of radionuclide diffusion and sorption in a granitic rock. J. Contam. Hydrol. 207, 8–16. https://doi.org/10.1016/j.jconhyd.2017.10.003.

Kahl, N., Dilissen, W.-A., Hidas, K., Garrido, C.J., López-Sánchez Vizcaíno, V., Román-Alpiste, M.J., 2017. 3-D microstructure of olivine in complex geological materials reconstructed by correlative x-ray μ-CT and EBSD analyses. J. Microsc. 268 (2), 193–207. https://doi.org/10.1111/jmi.12598.

Kelokaski, M., Siitari-Kauppi, M., Sardini, P., Möri, A., Hellmuth, K.-H., 2006. Characterisation of pore space geometry by 14C-PMMA impregnation- development work for in situ studies. J. Geochem. Explor. 90, 45–52. https://doi.org/10.1016/j.gexplo.2005.09.005.

Ketcham, R., Carlson, W., 2001. Acquisition, optimization and interpretation of X-ray computed tomographic imagery: applications to the geosciences. Comput. Geosci. 27, 381–400. https://doi.org/10.1016/S0098-3004(00)00116-3.

Ketcham, R., Slottke, D.T., Sharp, J.M., 2010. Three-dimensional measurement of frac-tures in heterogeneous materials using high-resolution X-ray computed tomography. Geosphere 6, 499–514. https://doi.org/10.1130/GES00552.1.

Kuva, J., Siitari-Kauppi, M., Lindberg, A., Aaltonen, I., Turpeinen, T., Myllys, M., Timonen, J., 2012. Microstructure, porosity and mineralogy around fractures in Olkiluoto bedrock. Eng. Geol. 139–140, 28–37. https://doi.org/10.1016/j.enggeo.2012.04.008.

Kuva, J., Voutilainen, M., Lindberg, A., Parkkonen, J., Siitari-Kauppi, M., Timonen, J., 2015a. Pore and mineral structure of rock using nano-tomographic imaging. MRS proceedings 1744, 235–240. https://doi.org/10.1557/opl.2015.335.

Kuva, J., Hellmuth, K.-H., Sardini, P., Siitari-Kauppi, M., 2015b. Verification of a simu-lation approach for estimating crack aperture using 14C-PMMA method. J. Coupled Syst. Multiscale Dyn. 3, 333–340. https://doi.org/10.1166/jcsmd.2015.1087.

Kuva, J., Voutilainen, M., Kekäläinen, P., Siitari-Kauppi, M., Timonen, J., Koskinen, L., 2015c. Gas phase measurements of porosity, diffusion coefficient, and permeability in rock samples from Olkiluoto bedrock, Finland. Transport Porous Media 107, 187–204. https://doi.org/10.1007/s11242-014-0432-2.

Kuva, J., Sammaljärvi, J., Parkkonen, J., Siitari-Kauppi, M., Lehtonen, M., Turpeinen, T., Timonen, J., Voutilainen, M., 2018. Imaging connected porosity of crystalline rock by contrast agent-aided X-ray microtomography and scanning electron microscopy. J. Microsc. 270, 98–109. https://doi.org/10.1111/jmi.12661.

Lai, J., Wang, G., Fan, Z., Chen, J., Qin, Z., Xiao, C., Wang, S., Fan, X., 2017. Three-dimensional quantitative fracture analysis of tight gas sandstones using industrial computed tomography. Sci. Rep. 7, 1825. https://doi.org/10.1038/s41598-017-01996-7.

Lalan, P., Dauzères, A., De Windt, L., Bartier, D., Sammaljärvi, J., Barnichon, J.-D., Techer, I., Detilleux, V., 2016. Impact of a 70°C temperature on an ordinary Portland cement paste/claystone interface: an in situ experiment. Cement Concr. Res. 83, 164–178. https://doi.org/10.1016/j.cemconres.2016.02.001.

Latief, F.D.E., Fauzi, U., Irayani, Z., Dougherty, G., 2017. The effect of X-ray micro computed tomography image resolution on flow properties of porous rocks. J. Microsc. 266, 69–88. https://doi.org/10.1111/jmi.12521.

Mazurier, A., Sardini, P., Rossi, A.M., Graham, R.C., Hellmuth, K.-H., Parneix, J.-C., Siitari-Kauppi, M., Voutilainen, M., Caner, L., 2016. Development of a fracture net-work in crystalline rocks during weathering: study of Bishop Creek chronosequence using X-ray computed tomography and 14C-PMMA impregnation method. GSA Bull. 128, 1423–1438. https://doi.org/10.1130/B31336.1.

Muuri, E., Ikonen, J., Matara-aho, M., Lindberg, A., Holgersson, S., Voutilainen, M., Siitari-Kauppi, M., Martin, A., 2016. Behavior of Cs in Grimsel granodiorite: sorption on main minerals and crushed rock. Radiochim. Acta 104, 575–582. https://doi.org/10.1515/ract-2015-2574.

Muuri, E., Siitari-Kauppi, M., Matara-aho, M., Ikonen, J., Lindberg, A., Qian, L., Koskinen, L., 2017. Cesium sorption and diffusion on crystalline rock: Olkiluoto case study. J. Radioanal. Nucl. Chem. 311, 439–446. https://doi.org/10.1007/s10967-016-5087-8.

Nilsson, K., Byegård, J., Selnert, E., Widestrand, H., Höglund, S., Gustafsson, E., 2010. Äspö Hard Rock Laboratory Long Term Sorption Diffusion Experiment (LTDE-SD): Results from Rock Sample Analyses and Modelling. Technical Report SKB R-10-68. SKB AB, Stockholm, Sweden.

Park, D.K., Ji, S.-H., 2018. Numerical simulation of anomalous observations from an in-situ long-term sorption diffusion experiment in a rock matrix. J. Hydrol 565, 502–515. https://doi.org/10.1016/j.jhydrol.2018.08.058.

Pittman, E., Thomas, J., 1979. Some applications of scanning electron microscopy to the study of reservoir rock. J. Petrol. Technol. 31, 1375–1380. https://doi.org/10.2118/7550-PA.

Poteri, A., Nilsson, K., Andersson, P., Byegård, J., Skålberg, M., Siitari- Kauppi, M., Helariutta, K., Voutilainen, M., Kekäläinen, P., Ikonen, J., Sammaljärvi, J., Lindberg, A., Kuva, J., Timonen, J., Koskinen, L., 2018. The First Matrix Diffusion Experiment in the Water Phase of the REPRO Project: WPDE 1, Working Report 2017-23. Posiva Oy, Olkiluoto, Finland.

Prêt, D., Sammartino, S., Beaufort, D., Fialin, M., Sardini, P., Cosenza, P., Meunier, A., 2010. A new method for quantitative petrography based on image processing of chemical element maps: Part II. Semi-quantitative porosity maps superimposed on mineral maps. Am. Mineral. 95, 1389–1398. https://doi.org/10.2138/am.2010.3433.

Robinet, J.C., Sardini, P., Coelho, D., Parneix, J., Prêt, D., Sammartino, S., Boller, E., Altmann, S., 2012. Effects of mineral distribution at mesoscopic scale on solute dif-fusion in a clay-rich rock: example of the Callovo-Oxfordian mudstone (Bure, France),

Water Resour. Res. 48, W05554. https://doi.org/10.1029/2011WR011352.

Robinet, J.C., Sardini, P., Siitari-Kauppi, M., Prêt, D., Yven, B., 2015. Upscaling the porosity of the Callovo-Oxfordian mudstone from the pore scale to the formation scale; insights from the 3H-PMMA autoradiography technique and SEM BSE imaging. Sediment. Geol. 321, 1–10. https://doi.org/10.1016/j.sedgeo.2015.02.007.

Sammaljärvi, J., Jokelainen, L., Ikonen, J., Siitari-Kauppi, M., 2012. Free radical poly-merisation of MMA with thermal initiator in brick and Grimsel granodiorite. Eng. Geol. 135–136, 52–59. https://doi.org/10.1016/j.enggeo.2012.03.005.

Sammaljärvi, J., Lindberg, A., Voutilainen, M., Kuva, J., Ikonen, J., Johanson, B., Siitari-Kauppi, M., Pitkänen, P., Koskinen, L., 2017. Multi-scale study of the mineral porosity of veined gneiss and pegmatitic granite from Olkiluoto, Western Finland. J. Radioanal. Nucl. Chem. 314, 1557–1575. https://doi.org/10.1007/s10967-017-5530-5.

Sardini, P., Moreau, E., Sammartino, S., Touchard, G., 1999. Primary minerals con-nectivity of polyphasic igneous rocks by high-quality digitalisation and 2D image analysis. Comput. Geosci. 25, 599–608. https://doi.org/10.1016/S0098-3004(98)00166-6.

Sardini, P., Siitari-Kauppi, M., Beaufort, D., Hellmuth, K.-H., 2006. On the connected porosity of mineral aggregates in crystalline rocks. Am. Mineral. 91, 1069–1080. https://doi.org/10.2138/am.2006.1939.

Sardini, P., Robinet, J.C., Siitari-Kauppi, M., Delay, F., Hellmuth, K.-H., 2007. Direct si-mulation of heterogeneous diffusion and inversion procedure applied to an out-dif-fusion experiment. Test case of Palmottu granite. J. Contam. Hydrol. 93, 21–37. https://doi.org/10.1016/j.jconhyd.2007.01.011.

Sardini, P., Kuva, J., Siitari-Kauppi, M., Hellmuth, K.-H., 2014. A simplified simulation approach for estimating crack aperture using 14C-PMMA method. J. Coupled Syst. Multiscale Dyn. 2 (4), 244–255. https://doi.org/10.1166/jcsmd.2014.1053.

Sardini, P., Caner, L., Mossler, P., Mazurier, A., Hellmuth, K.-H., Graham, R.C., Rossi, A.M., Siitari-Kauppi, M., 2015. Calibration of digital autoradiograph technique for quantifying rock porosity using 14C-PMMA method. J. Radioanal. Nucl. Chem. 303, 11–23. https://doi.org/10.1007/s10967-014-3617-9.

Sardini, P., Angileri, A., Descostes, M., Duval, S., Oger, T., Patrier, P., Rividi, N., Siitari-Kauppi, M., Toubon, H., Donnard, J., 2016. Quantitative autoradiography of alpha particle emission in geo-materials using the Beaver™ system. Nucl. Instrum. Methods A 833, 15–22. https://doi.org/10.1016/j.nima.2016.07.003.

Schladitz, K., 2011. Quantitative micro-CT. J. Microsc. 243, 111–117. https://doi.org/10.1111/j.1365-2818.2011.03513.x.

Schmitt, M., Halisch, M., Müller, C., Peres-Fernandes, C., 2016. Classification and quantification of pore shapes in sandstone reservoir rocks with 3-D X-ray micro-computed tomography. Solid Earth 7, 285–300. https://doi.org/10.5194/se-7-285-2016.

Siitari-Kauppi, M., 2002. Development of 14C-polymethylmethacrylate method for the characterisation of low porosity media: application to rocks in geological barriers of nuclear waste storage. Ph.D. thesis In: Report Series in Radiochemistry, vol. 17 University of Helsinki, Finland.

Toropainen, V., 2012. Core Drilling of REPRO Drillholes in ONKALO at Olkiluoto 2010-2011, Posiva Working Report 2012-26. Posiva Oy, Olkiluoto, Finland.

Trinchero, P., Molinero, J., Deissmann, G., Svensson, U., Gylling, B., Ebrahimi, H., Hammond, G., Bosbach, D., Puigdomenech, I., 2017. Implications of grain-scale mi-neralogical heterogeneity for radionuclide transport in fractured media. Transport Porous Media 116, 73–90. https://doi.org/10.1007/s11242-016-0765-0.

Turpeinen, T., Myllys, M., Kekäläinen, P., Timonen, J., 2015. Interface detection using a quenched-noise version of the EdwardsWilkinson equation. IEEE Trans. Image Process. 24, 5696–5705. https://doi.org/10.1109/TIP.2015.2484061.

Voutilainen, M., Siitari-Kauppi, M., Sardini, P., Lindberg, A., Timonen, J., 2012. Pore-space characterization of an altered tonalite by X-ray computed microtomography and the 14C-labeled-polymethylmethacrylate method. J. Geophys. Res. 117, B01201. https://doi.org/10.1029/2011JB008622.

Voutilainen, M., Sardini, P., Siitari-Kauppi, M., Kekäläinen, P., Aho, V., Myllys, M., Timonen, J., 2013. Simulated diffusion of tracer in altered tonalite with hetero-geneous distribution of porosity. Transport Porous Media. 96, 319–336. https://doi.org/10.1007/s11242-012-0090-1.

Voutilainen, M., Poteri, A., Helariutta, K., Siitari-Kauppi, M., Nilsson, K., Andersson, P., Byegård, J., Skålberg, M., Kekäläinen, P., Timonen, J., Lindberg, A., Pitkänen, P., Kemppainen, K., Liimatainen, J., Hautojärvi, A., Koskinen, L., 2014. In-situ experi-ments for investigating the retention properties of rock matrix in ONKALO, Olkiluoto, Finland. In: WM2014 Conference Proceedings, 14258. ISBN 978-0-9836186-3-8.

Voutilainen, M., Kekäläinen, P., Siitari-Kauppi, M., Sardini, P., Muuri, E., Timonen, J., Martin, A., 2017. Modeling transport of cesium in Grimsel granodiorite with micro-meter scale heterogeneities and dynamic update of Kd. Water Resour. Res. 53 (11), 9245–9265. https://doi.org/10.1002/2017WR020695.

Voutilainen, M., Sammaljärvi, J., Muuri, E., Donnard, J., Duval, S., Siitari-Kauppi, M., 2018. Digital autoradiography on C-14-labelled PMMA impregnated rock samples using the Beaver™. MRS Adv. 3, 1161–1166. https://doi.org/10.1557/adv.2018.226.

Widestrand, H., Byegård, J., Nilsson, K., Höglund, S., Gustafsson, E., Kronberg, M., 2010a. Long Term Sorption Diffusion Experiment (LTDE-SD): Performance of Main in Situ Experiment and Results from Water Phase Measurements. Technical Report SKB R-10-67. SKB AB, Stockholm, Sweden.

Widestrand, H., Byegård, J., Selnert, E., Höglund, S., Skålberg, M., Gustafsson, E., 2010b. Long Term Sorption Diffusion Experiment (LTDE-SD): Supporting Laboratory Program Sorption Diffusion Experiments and Rock Material Characterisation. Technical Report SKB R-10-66. SKB AB, Stockholm, Sweden.